First-principles theoretical analysis of magnetically tunable topological semimetallic states in antiferromagnetic DyPdBi

Anupam Bhattacharya,[1,2] Vishal Bhardwaj,[3] Meha Bhogra,[4] B. K. Mani,[5] Umesh V. Waghmare,[6] and Ratnamala Chatterjee[5,*]

[1]*Department of Mechanical Engineering, Indian Institute of Technology Delhi, New Delhi 110016, India*
[2]*Department of Physics and Astronomy, University of Manchester, Manchester M13 9PL, United Kingdom*
[3]*Department of Condensed Matter Physics, The Weizmann Institute of Science, Rehovot 7610001, Israel*
[4]*Department of Mechanical Engineering, Shiv Nadar University, Uttar Pradesh 201314, India*
[5]*Department of Physics, Indian Institute of Technology Delhi, New Delhi 110016, India*
[6]*Theoretical Sciences Unit, Jawaharlal Nehru Centre for Advanced Scientific Research, Bengaluru 560064, India*

(Received 27 February 2022; revised 20 December 2022; accepted 24 January 2023; published 21 February 2023)

A number of compounds in the family of rare-earth half-Heusler alloys have been predicted to be topologically nontrivial semimetals, classified as Weyl, triple-point, and Dirac semimetals based on the multiplicity of degeneracy of the nodal points or crossing of linearly dispersed electronic bands. Here, we present a first-principles theoretical characterization of the electronic topology of the antiferromagnetic half-Heusler alloy DyPdBi. In the antiferromagnetic state preserving C_{3v} symmetry of the crystal, DyPdBi is a triple-point semimetal hosting four triply degenerate nodes along the threefold symmetry axis of the Brillouin zone. In contrast, the antiferromagnetic state of DyPdBi with local magnetic moments on Dy rotated to a direction perpendicular to the C_3 axis breaks the threefold rotational symmetry, and hosts four Weyl nodes in its Brillouin zone. Our calculations of the Berry curvature of their electronic states clearly show that the triple-point fermions of DyPdBi exhibit a signature peak in the anomalous Hall conductivity, while the Weyl fermions do not contribute to anomalous Hall conductivity. As these two topologically distinct magnetic states are separated by a small energy difference of ≈15 meV, we expect them to be switchable with a magnetic field or spin torque and distinguishable experimentally from anomalous Hall conductance.

DOI: 10.1103/PhysRevB.107.075144

I. INTRODUCTION

Almost a decade ago, many rare-earth half-Heusler alloys were identified as topologically nontrivial materials with metallic and semimetallic electronic structures [1–4]. Shortly thereafter, experimental studies confirmed that the topological semimetals form a class of interesting materials which provide a platform for realizing elusive quasiparticles such as Dirac, Weyl, and Majorana fermions [5–9]. These studies stimulated research activity to characterize topological half-Heusler alloys based on the degeneracy of topologically protected nodes with the aim of identifying these quasiparticles. Triple-point semimetallic phases were identified in diamagnetic rare-earth half-Heusler alloys such as LuPtBi, LaPtBi, and YPtBi [10]. Some studies on paramagnetic [11–13] and ferromagnetic [14] (under external magnetic field) phases in GdPtBi identified triple-point and Weyl semimetallic states, respectively. Another study based on a model Hamiltonian approach reported the possibility of the existence of different topological phases (Weyl, Dirac, triple point, topological insulating states, etc.) in the antiferromagnetic (AFM) phase of half-Heusler alloys [15].

Quasiparticles such as Weyl and triple-point fermions express themselves through several exotic quantum transport phenomena such as chiral anomaly, Fermi arcs, planar Hall effect, and large intrinsic anomalous Hall effect (AHE) [13,14,16–20]. However, there is no simple, definitive way to differentiate a triple-point semimetal from a Weyl semimetal, except through the detection of Fermi arcs by angle-resolved photoemission spectroscopy (ARPES). This will be facilitated if there is a material system that can switch between these topological states, which can be probed with transport experiments.

DyPdBi exhibits an AFM ordering with $T_N = 3.5$–4.0 K [21,22] in polycrystalline form and $T_N = 2.7$ K in its single-crystalline form [23]. It was recently reported to show promising characteristics for hosting topologically protected crossings of bands. An indication of topological nontrivial states in DyPdBi thin films oriented along the [110] direction is experimentally observed in the form of weak-antilocalization and Shubnikov–de Haas oscillations [24,25]. Another recent experimental work on paramagnetic DyPdBi single crystals reported observations of negative magnetoresistance and planar Hall effect, which was partially attributed to the chiral anomaly and is suggestive of the existence of a Weyl semimetallic phase in the paramagnetic structure [19].

It is desirable to develop an understanding of the electronic structure and topological phases of this antiferromagnetic material. In this work, we use density-functional-theory-based first-principles calculations with a goal to determine its electronic structure and topological signatures, and a possible switchability between its distinct topological states, if any.

*Corresponding author: ratnamalac@gmail.com

More precisely, we use first-principles and group-theoretical analysis to address the following questions: (i) What is the electronic structure of DyPdBi at a low-temperature antiferromagnetic state? (ii) Are topologically nontrivial electronic states possible in AFM-DyPdBi? (iii) Can the electronic structure of DyPdBi calculated from first principles be reproduced with a model Hamiltonian derived using group theory? (iv) Are its topological electronic states tunable and, possibly, switchable? (v) Are there any transport signatures of these states that can be seen experimentally?

II. FIRST-PRINCIPLES METHODS

Our first-principles calculations are based on density functional theory (DFT) and the use of the plane-wave basis in the representation of Kohn-Sham wave functions and charge density. We have used a combination of two implementations of DFT, i.e., VASP and QUANTUM ESPRESSO, for internal consistency checks and also to benefit from their different capabilities. Full structural relaxation of antiferromagnetic DyPdBi is carried out using the Vienna *Ab initio* Simulation Package (VASP) [26–28] until the interatomic forces reduce below 0.02 eV/Angstrom in magnitude, corresponding to a local minimum of energy. For this relaxed structure, we use the QUANTUM ESPRESSO (QE) [29,30] package for a set of self-consistent field (SCF) and non-self-consistent field (NSCF) calculations to determine the electronic structures and relevant properties of DyPdBi. The plane-wave basis for the representation of Kohn-Sham wave functions was truncated with an energy cutoff of 385 eV in our VASP calculations, and with a cutoff of 120 Ry in our QE calculations. A uniform $9 \times 9 \times 9$ mesh of k points was used in sampling integrations over the Brillouin zone (BZ). We use noncollinearly ordered states of spins, including relativistic effects with a spin-orbit interaction term. Within QUANTUM ESPRESSO, for Dy, norm-conserving pseudopotentials from the PSlibrary [31] were used because it was found to be optimal in terms of the convergence and reproduction of electronic states obtained from the projector augmented-wave (PAW)-based calculations with VASP. For Bi and Pd, optimized norm-conserving Vanderbilt (ONCV) pseudopotentials from the Pseudo-dojo library [32] have been used. A benchmark study of the ONCV pseudopotentials in comparison with all-electron calculations was reported by Lejaeghere *et al.* [33].

Since Dy occurs in a +3 nominal oxidation state in DyPdBi, it possesses 5 μB spin magnetic moments per Dy atom. We have included this in a self-consistent manner by including $4f$ electrons in the valence. We consider two noncollinearly ordered spin states: an antiferromagnetic state with spins along the C_3 axis [AFM-||, Fig. 1(a)] and one with spins perpendicular to the C_3 axis [AFM-$\perp$, Fig. 4(a)]. The exchange-correlation energy of electrons is treated with a generalized gradient approximation (GGA) as formulated in the energy functional of Perdew, Burke, and Ernzerhof (PBE) [34]. We treat the on-site electron correlations of the f electrons of Dy using the Hubbard U parameter, $U = 5$ eV, a value optimized to reproduce the experimental magnetic moment of Dy [21,35], which is also consistent with +3 oxidation state of Dy in Ref. [36].

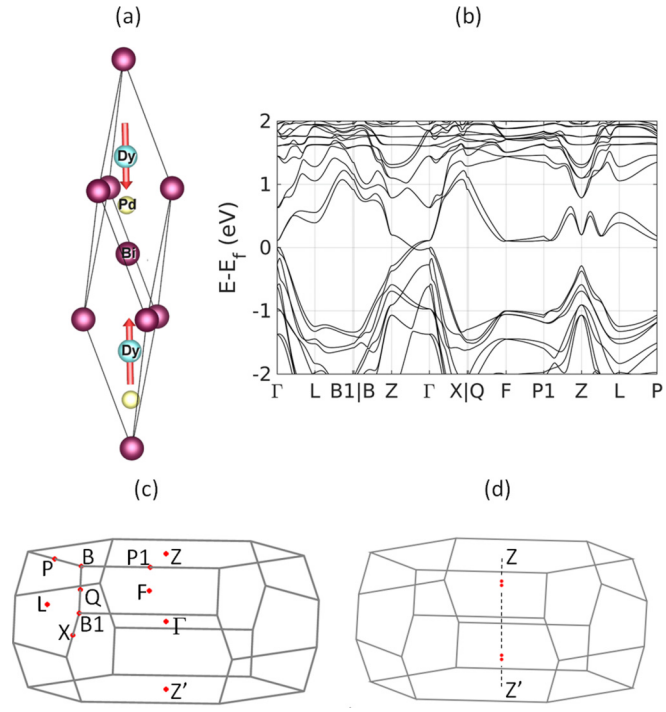

FIG. 1. (a) Primitive unit cell of DyPdBi in crystal structure with symmetry of space group $R3m$ and antiferromagnetically ordered spins of Dy along the C_3 axis (AFM-||), (b) its electronic structure calculated with inclusion of the SOC, (c) corresponding Brillouin zone with high-symmetry k points, and (d) locations of the triple-point nodes in the BZ.

We used maximally localized Wannier functions (MLWFs) [37,38] to derive a tight-binding model in the determination of the (100) surface electronic structure of DyPdBi, modeled as a semi-infinite slab. With the postprocessing WANNIER90 and WANNIER BERRI packages, we computed the Berry curvature Ω and the intrinsic anomalous Hall conductivity (AHC) within the Kubo-Greenwood formula,

$$\sigma_{\alpha\beta} = -\frac{e^2}{\hbar}\frac{1}{n_k V_c}\sum_k \Omega_{\alpha\beta}(k). \tag{1}$$

Here, α and β are two mutually perpendicular directions, n_k is the total number of K points, V_c is the volume of the unit cell, and $\Omega_{\alpha\beta}(k)$ is the Berry curvature.

III. RESULTS AND DISCUSSIONS

A. Crystal structure of DyPdBi

DyPdBi is an antiferromagnetic half-Heusler alloy with a face-centered-cubic ($F\bar{4}3m$) lattice structure with cubic lattice parameter 6.6343 Å observed experimentally [35], and its antiferromagnetic structure involves spin ordering with a [1/2,1/2,1/2] wave vector [23] having a cell-doubled periodicity. As our first-principles calculations employ periodic boundary conditions, we use a periodic cell with two DyPdBi formula units, i.e., a six-atom unit cell with space group $R3m$ [see Fig. 1(a), along with the corresponding Brillouin zone and relevant high-symmetry points in Fig. 1(b)]. Our calculated estimate of the cubic lattice parameter is 6.740 Å,

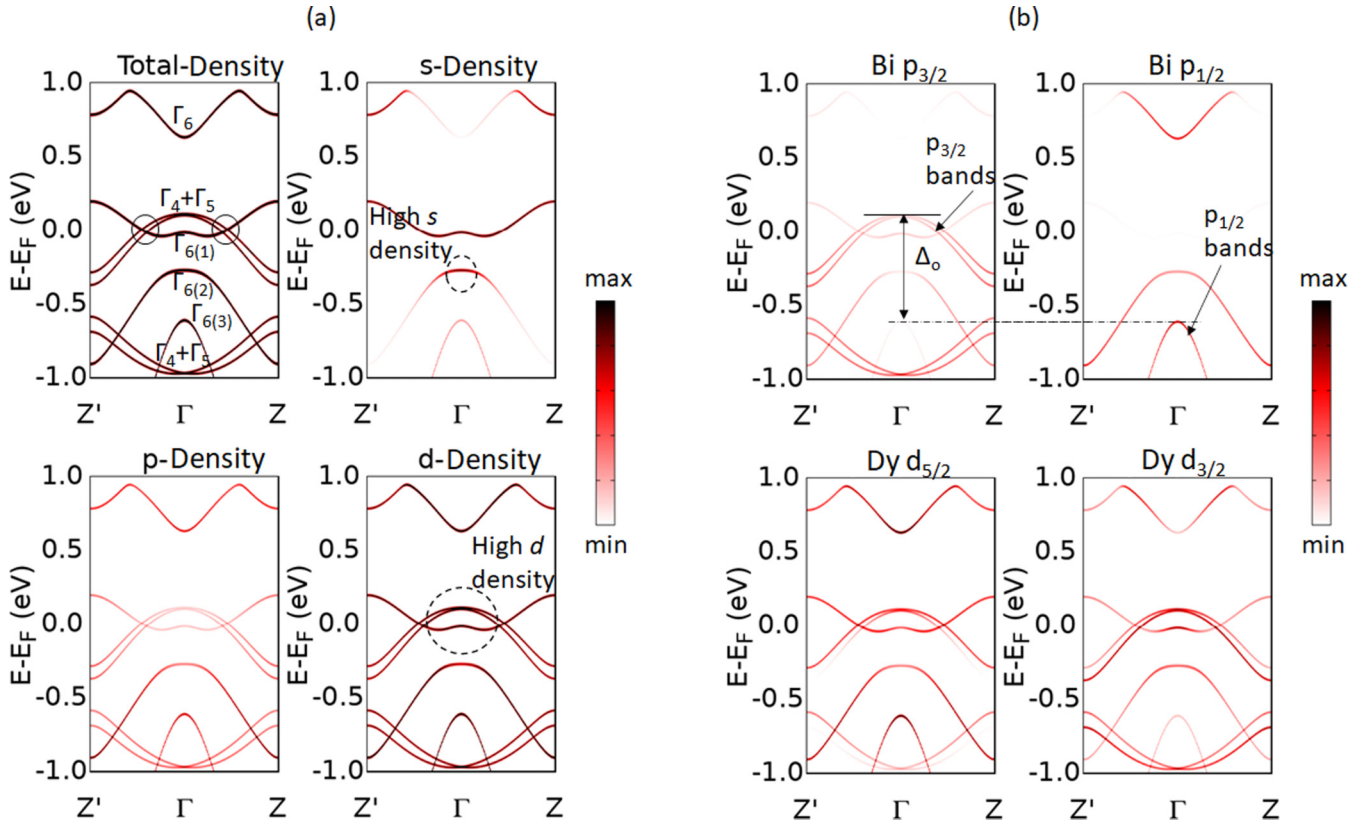

FIG. 2. (a) Total and orbital projected band structure along $Z-\Gamma-Z'$ showing contributions of s, p, and d orbitals and (b) spin-orbit split bands constituted of p orbitals of Bi (top panels) and of d orbitals of Dy (bottom panels). These results have been obtained with the kresolved_dos module of the QE package.

which lies within the typical range of GGA overestimates with respect to its experimental value.

B. Electronic structure of AFM-|| state of DyPdBi with magnetic moments along [111]

1. Electronic band dispersion and topological nodal points

The electronic structure, calculated at the optimized lattice of AFM-|| DyPdBi and with inclusion of the spin-orbit coupling (SOC) [see Fig. 1(b)] reveals two points along the $Z-\Gamma$ direction, at which its linearly dispersed valence and conduction bands cross at energies close to the Fermi level. In the rest of the BZ, they stay apart and are separated by a gap. To understand the nature of these crossings and probe any possibility of a band inversion, we examine the electronic structure along $Z'-\Gamma-Z$ in detail, which is shown in Fig. 2.

We first examine the electronic structure and orbital-projected bands showing k-resolved projected densities of s, p, and d orbitals of DyPdBi along the $Z'-\Gamma-Z$ lines [see Fig. 2(a)]. The contribution of f orbitals of Dy is weak and hence is not shown. In the vicinity of Fermi energy, a negative-curvature doubly degenerate band at Γ, $\Gamma_4+\Gamma_5$, emerges at $\approx$0.1 eV above the Fermi energy and extends down below the Fermi energy, splitting into two nondegenerate bands, away from Γ. These bands have mixed $p-d$ character (see panels p-Density and d-Density, respectively), with dominant contributions from the Bi $-$ p and Dy $-$ d orbitals. Another relevant band in the vicinity of the Fermi energy is the doubly degenerate $\Gamma_{6(1)}$ band. In contrast to the $\Gamma_4+\Gamma_5$ band, it starts just below Fermi energy and extends into the conduction band as k varies away from the Γ. This leads to four symmetry-protected triple-point crossings [shown in white circles in Total-Density of Fig. 2(a)] along the C_3 axis close to the Fermi energy. These triply degenerate nodes are protected by the C_{3v} point group symmetry of the magnetic structure. The energy dispersion around these triple nodal points constitutes an upright conical structure, and hence resembles the type-I triple points. The precise locations of these crossing points in the BZ are identified by non-self-consistent field (NSCF) calculations on a dense mesh around these points and are shown as red dots in Fig. 1(d), and their k coordinates are given in Table I.

To get further insight into the nature of band inversion, we calculated band structures projected onto spin-orbit (SO) split orbitals, $p_{1/2}$ and $p_{3/2}$ of bismuth and $d_{3/2}$ and $d_{5/2}$ of dysprosium, which are shown in Fig. 2(b). The d orbitals of palladium have negligible contributions and hence are not shown. In the upper two panels, we note a large spin-orbit splitting of bands of Bi-p orbitals, which leads the two states $p_{3/2}$ (four bands of $\Gamma_4+\Gamma_5$ and $\Gamma_{6(1)}$ symmetry) and $p_{1/2}$ ($\Gamma_{6(3)}$ band) to be separated from each other. The splitting energy Δ_0 is $\approx$0.722 eV and is comparable with the splitting energies in other Heusler alloys [39]. As shown in the top-right panel of Fig. 2(a), the other band $\Gamma_{6(2)}$, between the $\Gamma_{6(3)}$ and $\Gamma_{6(1)}$ bands, has a dominant s character near the Γ point. The SO splitting of Bi $-$ p orbitals allows the $\Gamma_4+\Gamma_5$

TABLE I. Locations (k, ϵ) of nodes of the crossing of linearly dispersed bands, the triple and Weyl points, in DyPdBi. ΔE represents their energies in eV with respect to the Fermi energy.

Location in the BZ (reduced coordinates)	ΔE (eV)
AFM-||	Triple points
(0.227, 0.227, 0.227)	0.006
(0.202, 0.202, 0.202)	−0.013
(−0.202, −0.202, −0.202)	−0.013
(−0.227, −0.227, −0.227)	0.006
AFM-⊥	Weyl points
(0.008, 0.076, 0.060)	0.004
(0.008, 0.059, 0.075)	0.004
(−0.008, −0.060, −0.076)	0.004
(−0.008, −0.075, −0.059)	0.004

band to be higher in energy than the s-type $\Gamma_{6(2)}$ band, leading to a $s-p$ band inversion. Similar band inversions are also observed in other half-Heusler alloys such as YPtBi [40]. The band-inversion energy, $\Delta E_\Gamma = [\Gamma_{4+5} - \Gamma_6(2)]$, in DyPdBi is estimated to be ≈0.383 eV. We note from the lower two panels of Fig. 2(a) that although the band inversion is driven by the strong SO splitting of Bi-p orbitals, the dominant contribution to the $\Gamma_4 + \Gamma_5$ band is from the Dy-d orbitals. This large contribution from d electrons compelled us to investigate the role of d-orbital splitting in the band inversion. For this, we computed the densities of projections onto the $d_{3/2}$ and $d_{5/2}$ orbitals of dysprosium [see the bottom two panels of Fig. 2(b)]. It is evident that none of the densities of these orbitals vanish at the Γ point. This reveals that the band inversion at Γ is not affected by the splitting of d orbitals.

The nature of dispersion of the frontier bands is further elucidated with group-theoretical calculations, presented in detail in the Supplemental Material [41]. The four frontier bands of $p_{3/2}$ nature are responsible for the triply degenerate crossings and hence we study these four bands using $k \cdot p$ perturbation theory following Ref. [15]. Under the C_{3v} point-group symmetry of the AFM-|| state, the fourfold degeneracy of the $p_{3/2}$ orbitals is further split into a twofold $\Gamma_{6(1)}$ and nondegenerate Γ_4 and Γ_5 bands with an energy gap of 0.127 eV. Second, the $\Gamma_{6(1)}$ bands have low bandwidth and exhibit a recurve-bow-like feature around Γ, signifying its nonparabolic nature. We find that this nonparabolicity of the bands can be incorporated in the $k \cdot p$ perturbation model by introducing correction terms for interband coupling using Löwdin partitioning. However, we find that the $\Gamma_{6(1)}$ bands exhibit high-order polynomial dispersion, which makes an accurate representation of these bands away from Γ within $K \cdot P$ theory difficult. The details of the partitioning technique and parameters of the fourth-order polynomial approximation are given in the Supplemental Material [41]. More importantly, the curvature of the frontier bands of DyPdBi has opposite sign to that suggested in Ref. [15], resulting from the opposite sign of the fitting parameters C_k and ϵ (Ref. [15]).

2. *Surface electronic structure and topological Fermi arcs*

The Fermi arc formed on the surface electronic states constitutes a signature of topologically nontrivial semimetallic

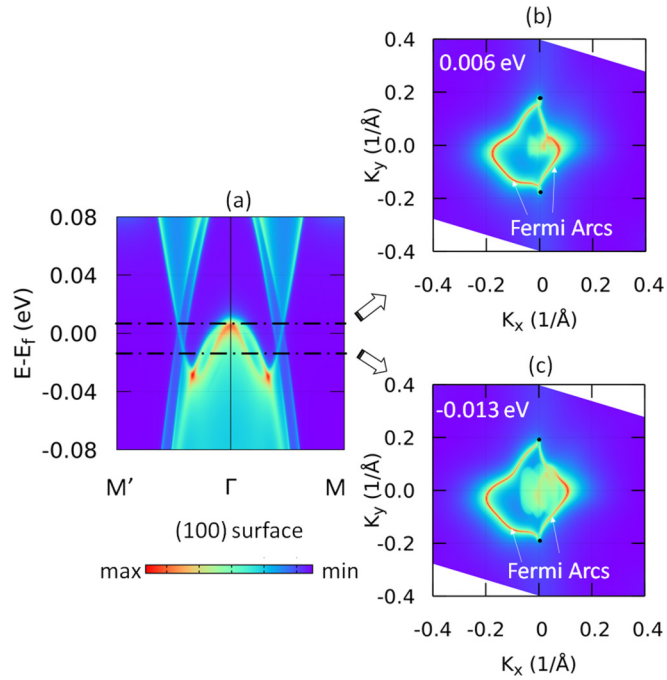

FIG. 3. Electronic structure of the Dy-terminated (100) surface of AFM-|| DyPdBi calculated using a Wannier-functions-based tight-binding model with the WANNIER90 and WANNIERTOOLS packages, displayed as contour plots of k-resolved density of states (a) in which the nodal points and conical band structural features at 0.006 and −0.013 eV are marked by dash-dotted lines. Curves in reciprocal space marking k points (black dots) at which bands in the surface electronic structure occur at energies (b) 0.006 eV and (c) −0.013 eV, obtained from the density of states projected onto surface atoms of the semi-infinite slab. K_x and K_y are two mutually perpendicular axes on the 2D BZ.

fermions. The endpoints of such an arc are the projection of the Weyl or topological nodal points in the bulk electronic structure onto the surface Brillouin zone. Only at these k points can the surface states spill into the bulk. For triple-point fermions in particular, the projection of each triple point acts as the origin of two Fermi arcs [10]. Therefore, next we calculate and analyze the electronic structure of DyPdBi semi-infinite slabs to identify the Fermi-arc-like surface states. For this, we simulated a (100)-terminated semi-infinite slab consisting of 50 layers of AFM-|| DyPdBi unit cells, using a tight-binding model derived from Wannier functions as the localized basis.

The k-resolved density of states, showing the contribution of electrons from the bulk of the semi-infinite slab, is shown in Fig. 3(a). We find four Dirac-cone-like structures along the $M'(0.0, -0.5) - \Gamma - M(0.0, 0.5)$ lines, similar to Fig. 2, two of which are at the energy ≈0.006 eV and the other two at ≈ −0.013 eV, with respect to the Fermi energy (marked by two black dash-dotted lines). To locate the Fermi arcs, we calculated the electronic states on the Dy-terminated slab surface and projected the isoenergy electron density on the two-dimensional (2D) BZ at these two energies; see Figs. 3(b) and 3(c), respectively. We find two Fermi-arc surface states, connecting the triple points (marked by black dots). This confirms the existence of topologically nontrivial triple-point

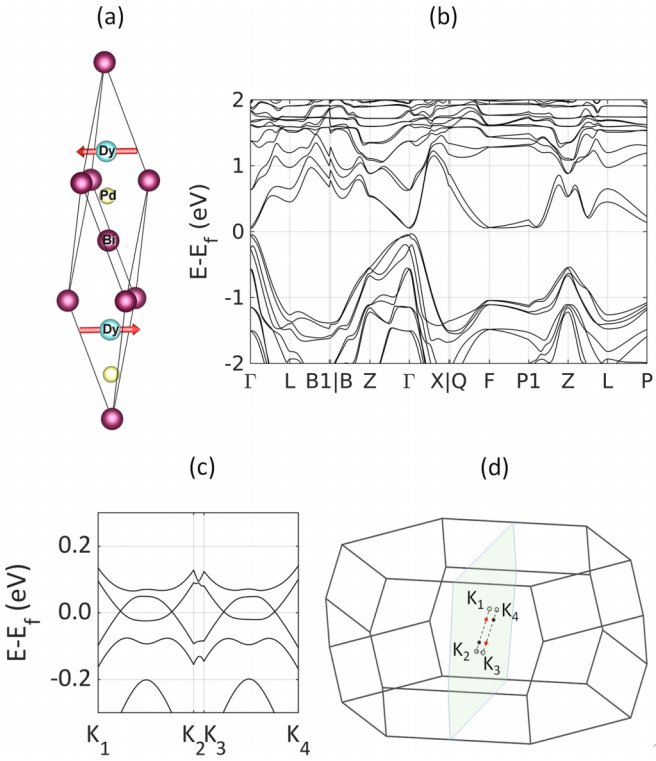

FIG. 4. (a) Structural unit of the AFM-⊥ state of DyPdBi with magnetic moments (spins of Dy) oriented perpendicular to the [111] axis. (b) Its electronic structure calculated along high-symmetry lines shows an apparent gapped bulk state, (c) while that along lines of low symmetry reveals Weyl points. (d) The locations of these four Weyl points are indicated as dots in the BZ. Red and black colored dots denote Weyl points of +1 and −1 chirality.

fermions in antiferromagnetic DyPdBi with magnetic moments of Dy along the [111] direction. Details of the Fermi-arc connectivity on the other surfaces are presented in the Supplemental Material [41].

C. Electronic structure of AFM-⊥ state of DyPdBi with magnetic moments perpendicular to [111]

In the previous section, we discussed the electronic structure of the AFM-|| state of DyPdBi with magnetic moments oriented along the [111] direction. Now, we investigate the electronic structure of the AFM-⊥ state of DyPdBi, which is the case when magnetic moments are oriented perpendicular to [111] (and along the $[\bar{1}\bar{1}2]$ direction of the cubic unit cell). The corresponding unit cell is shown in Fig. 4(a). We note that the magnetic structure remains a G-type AFM with a [1/2, 1/2, 1/2] magnetic wave vector. This AFM-⊥ structure is found to be energetically less stable, with the calculated total energy ≈15 meV (per formula unit) more than that of the AFM-|| state. Since the two AFM phases are energetically very close to each other, we expect them to be switchable. We assume that the magnetic potential energy associated with the dipole moment on each Dy atom has to be at least 15 meV to be able to rotate the moment to a perpendicular orientation; thus the required magnetic field can be estimated to be approximately 13 Tesla. Such magnetic switching with magnetic fields was recently reported in a similar material, DyPtBi [42], where antiferromagnetic moments switch alignment between two spin configurations while retaining the antiferromagnetic wave vector, under a magnetic field <4 T. This is also in agreement with our finding that the magnetic anisotropy in these materials is small enough to enable easy switching. Similar switching using spin torques is reported in the literature [43–45] as well.

1. Band dispersion and topologically protected crossings

In the AFM-⊥ state, deviation in the orientation of the magnetic moments from the C_3 symmetry axis reduces the symmetry (C_{3v} point group) of AFM-||. In this state, only a mirror symmetry with mirror plane passing through [111] remains, with the symmetry group $C_s(C_{1h})$. Electronic band dispersion of the AFM-⊥ state of DyPdBi, shown in Fig. 4(b), reveals a gap along the high-symmetry points. Upon detailed inspection of the lines of low symmetry in the BZ [along K_1 (0.015, 0.137, 0.121)– K_2 (−0.015, −0.120, −0.134)– K_3 (−0.015, −0.129, −0.114)– K_4 (0.015, 0.123, 0.137) lines], however, we find that there are four Weyl crossings [shown as red and black dots in the Fig. 4(d)] and they fall on either side of the vertical mirror plane going through $k_2 = k_3$ [the green plane in Fig. 4(d)]. The red and black colors represent +1 and −1 chirality of the Weyl nodes, respectively. The emergence of these nodes is attributed to broken threefold rotational symmetry. The locations of these nodes are given in Table I. Upon further inspection, we find that the electronic dispersion around these Weyl points forms inclined conical structures, with characteristics of a type-I topological semimetal.

To determine the nature of the band inversion, we study the orbital-projected band structures of the s, p, and d orbitals shown in Fig. 5. Similar to the case of AFM-|| DyPdBi, the d-orbital density is high throughout the energy range (bottom-right panel). However, the distribution of the s-orbital density in the top-right panel and p-orbital density in the bottom-left panel reveals that the $p_{3/2}$ state lies at higher energy than the s state, indicating the $s - p$ band inversion like the AFM-|| state.

Our analysis of the electronic structure of the AFM-⊥ state using group theory is available in the Supplemental Material [41]. We obtained the frontier $p_{3/2}$ bands solving the $k \cdot p$ perturbation-theory-based Hamiltonian numerically. Comparing these bands with the AFM-|| phase, it is clear that the doubly degenerate bands have higher energy than the nondegenerate bands. This ordering is opposite to the bands of AFM-|| state and yields the opposite sign of the fitting parameters C_k, $e_{3/4/5}$, and γ_3 along the $k_x = k_y = k_z$ line. Under this C_{1h} point group of the magnetic Hamiltonian, the doubly degenerate $p_{3/2}$ bands split by a tiny energy into two nondegenerate bands at k away from Γ. This splitting is very weak along the $Z' - \Gamma - Z$ line as shown in Fig. 5 and Fig. 1(b) of the Supplemental Material [41]. We find that the locations of the Weyl nodes are on both sides of the vertical mirror plane which match the symmetry properties of the Weyl points predicted in Ref. [15]. However, the nature of dispersion modeled with even quartic polynomials cannot accurately reproduce the dispersion of the frontier bands calculated within DFT. In a nutshell, although the symmetry properties of the frontier

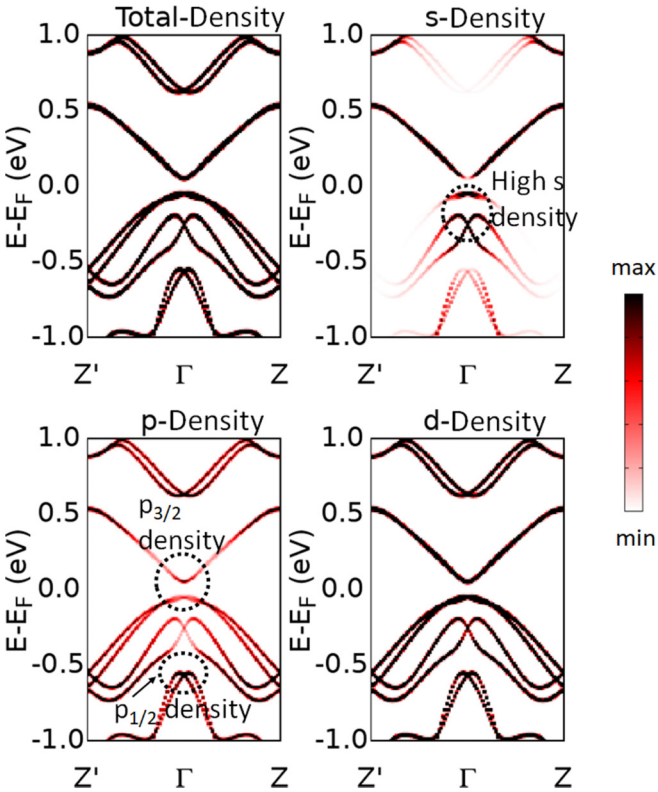

FIG. 5. Total and orbital projected band structure of AFM-⊥ showing combined contributions of the *s*, *p*, and *d* orbitals of Dy, Pd, and Bi atoms to bands near the gap or Weyl points.

bands agree with the group-theoretical analysis, the nonlinear dispersion of bands is not captured well by the $k \cdot p$ model.

2. Surface electronic structure and topological Fermi arcs

A semi-infinite slab of the AFM-⊥ state of DyPdBi, consisting of 50 unit cells and terminated along (100), was simulated to extract the Fermi-arc surface states on the Dy-terminated surface. The isoenergy electronic density at energy 0.004 eV, showing the contributions of the surface atoms of the slab, is shown in Fig. 6(a). The locations of the Weyl nodes after their projection on the 2D BZ are represented by red and black dots for $+1$ and -1 chirality, respectively. In contrast to the triple-point phase, here we observe only *one* Fermi arc originating at each node [10]. This clearly indicates the Weyl semimetallic phase, with a distinct topological character of the same material. Connectivity between the Weyl nodes on other surfaces is presented in the Supplemental Material [41].

To determine the nature of the electronic dispersion of the slab, we calculated the *k*-resolved density of states along the lines that pass through the Weyl nodes. Figure 6(b) shows the *k*-resolved density of states along K_a-K_b line, where $K_a = (-0.017, 0.5)$ and $K_b = (-0.017, -0.5)$. As expected, the $E - k$ dispersion is linear. The electronic dispersion through the other pair of Weyl points is similar and hence not shown.

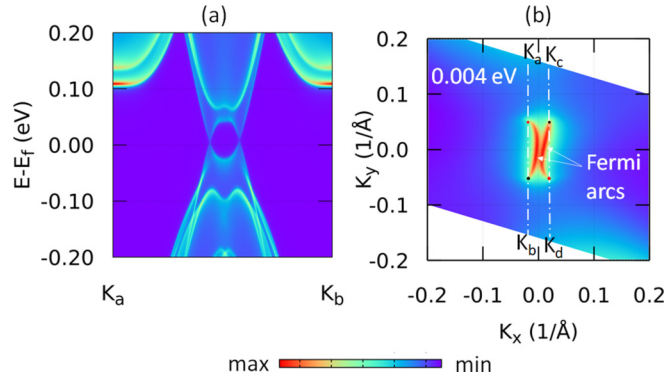

FIG. 6. (a) Electronic structure of the Dy-terminated (100) surface of AFM-⊥ DyPdBi calculated using the Wannier-functions-based tight-binding model with the WANNIER90 and WANNIERTOOLS packages, displayed as contour plots of *k*-resolved density of states in which the nodal points and conical band structural features are evident. (b) Fermi arcs, the curves in reciprocal space marking *k* points at which bands in the surface electronic structure occur at energies 0.004 eV obtained from the density of states projected onto surface atoms of the semi-infinite slab.

D. Characteristic difference between Weyl and triple-point fermions identified through AHC

Since DyPdBi hosts two topological semimetallic states, it is intriguing to examine the difference in their transport properties. Recently, a few works reported anomalous Hall effects of topological semimetallic structures in Heusler alloys [14,20,42,46–48]. Here, we compare the anomalous Hall signatures of triple-point and Weyl semimetallic states of DyPdBi, using symmetry analyses (in the Supplemental Material [41]) and first-principles calculations.

Since we studied a pure and compensated antiferromagnet without any external magnetic field, we report the intrinsic AHC only from first principles. The intrinsic AHC is calculated using the Kubo-Greenwood formula, given by Eq. (1), where the Berry curvature has been determined using WANNIER90 and WANNIER BERRI software [49]. To test the convergence of the AHC computation, we performed a series of calculations with increasing resolution of the *k* mesh, and the data on AHC reported here are based on calculations with a fine *k* mesh of $700 \times 700 \times 700$ points.

Figure 7(a) shows the Berry curvature and intrinsic AHC for the triple-point semimetallic phase of DyPdBi. The center panel shows the electronic band structure along the $Z' - \Gamma - Z$ line, where the red to blue colors in the band represent the spin polarization of the states. For easy reference, peaks originating from different features of the accompanying band structure are marked as 1, 2, and 3 in orange circles. Here, each triple point gives rise to two peaks of opposite signs (the logarithmic plot shows only the magnitude) in Berry curvature around it. Two peaks of the Berry curvature from each of the adjacent triple-point pairs merge into one in the middle, leading to a total of six distinguishable peaks in the bottom panel of Fig. 7(a). Also, in agreement with the symmetry analysis of AHC (presented in the Supplemental Material [41]), only the σ_{xy} component of AHC is nonzero. Since triple points act both as the source and sink of the curvature without a fixed Chern

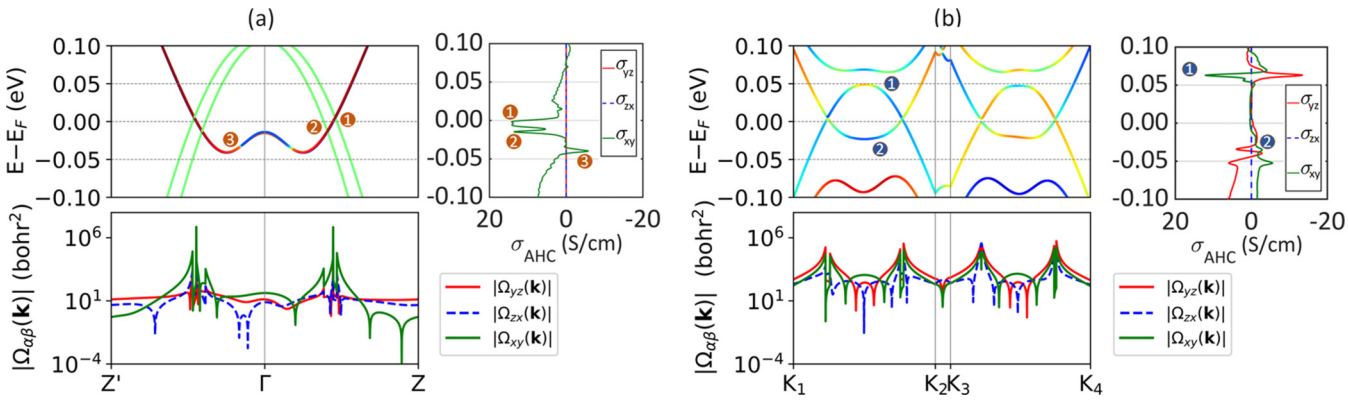

FIG. 7. Origin of intrinsic AHC in the (a) triple-point semimetallic AFM-|| and (b) Weyl semimetallic AFM-⊥ phases of DyPdBi. The top-left panels show electronic bands through the topologically protected nodes along with their spin character. The top-right panels show anomalous Hall conductivity as a function of energy. The bottom panels show Berry curvature $\Omega_{\alpha\beta}(k)$ along $Z' - \Gamma - Z$, summed over the occupied bands. σ_{AHC} and Ω have been obtained with the WANNIER90 and WANNIER BERRI packages.

number to quantify the Berry flux around it, peaks in the Berry curvature do not cancel each other and lead to peaks in the intrinsic AHC at triple-point crossings. These are represented as peaks 1 and 2 and are found to be of approximately the same magnitudes of about 14 S/cm. The other peak, peak 3, is due to the spin flipping in the band structure, which arises from the change in orbital character and subsequent twists in the wave functions in the momentum space. Here we note that nonvanishing AHC has been reported in compensated antiferromagnets experimentally [50,51], e.g., in half-Heusler GdPtBi and inverse Heusler Ti_2MnAl.

In Fig. 7(b), we present intrinsic AHC along with magnitudes of Berry curvature and electronic band structure along the K_1-K_2 and K_3-K_4 paths for the Weyl semimetallic phase of DyPdBi. The σ_{xy} and σ_{yz} components are nonzero, in agreement with the symmetry analysis presented in the Supplemental Material [41]. In the reciprocal space lattice, K_1, K_2, K_3, and K_4 are at (0.015, 0.137, 0.121), (−0.015, −0.120, −0.134), (−0.015, −0.129, −0.114), and (0.015, 0.123, 0.137) reduced coordinates, respectively. Each of the crossings show two peaks of approximately the same magnitude in the Berry curvature, with one on each side. Since Weyl nodes are either pure source or sink of the Berry curvature, the Berry curvatures on two sides of the crossings have opposite phase. This leads to cancellation of the net Berry curvature, giving rise to a negligible AHC at the Fermi energy, shown in the rightmost panel of the figure. Nonvanishing AHC arises from avoided crossings, and spin flipping [see peaks 1 and 2 in Fig. 7(b), respectively] is seen at energies above and below the Fermi energy. Since DyPdBi does not have other bands at the Fermi energy, the vanishing AHC response at the Fermi energy implies that the Weyl nodes do not contribute to AHC. This is significantly different from that of the triple-point semimetallic state.

Our results of vanishing AHC in the Weyl semimetallic state are consistent with the reported intrinsic AHC in TbPtBi [47] in its magnetic-field-induced ferromagnetic Weyl phase. Although a large AHC is reported, it is attributed to the anticrossing of the spin-split bands near the Fermi energy, and not to the Weyl nodes which show a negligible contribution. Recent experimental studies have suggested that in DyPtBi, AHC is governed by magnetically driven topological transitions [42,48], which is directly observed in the current study. Moreover, since the energy difference between the two observed magnetic configurations of DyPdBi is very small, the application of even a small magnetic field can introduce some degree of spin canting and associated nonvanishing Berry curvature, and that can lead to an enhanced AHC [52].

IV. CONCLUSIONS

We presented an analysis of the electronic structure and topological properties of antiferromagnetic DyPdBi using density-functional-theory-based first-principles calculations and group theory. We find that the AFM-|| state with magnetic moments oriented along [111] is more stable, with energy of ≈15 meV lower than the AFM-⊥ state with magnetic moments perpendicular to [111]. Both the AFM states of DyPdBi exhibit an electronic structure with topologically nontrivial linearly dispersed band crossings: triple-point semimetallic phase of AFM-|| and Weyl semimetallic phase of AFM-⊥. They exhibit a remarkable contrast in their anomalous Hall conductivity responses: triple-point fermions in AFM-|| exhibit peaks in AHC, while Weyl nodes of AFM-⊥, being just above the Fermi energy, give a vanishing AHC response. As AFM-|| and AFM-⊥ states of DyPdBi are separated by a small energy, we think switching between the two with a magnetic field or spin torque could open up switchable distinct topological states for novel quantum technological devices.

ACKNOWLEDGMENTS

A.B. acknowledges Prof. J. K. Dutt, IIT Delhi and A. Toshniwal, EPFL for valuable suggestions, as well as MHRD India and the Commonwealth Scholarship Commissions in the UK for financial support. R.C. acknowledges the financial assistance received from Grant No. K2-2022-022 from NUST "MISIS" Russia, DST Nanomission Project

No. DST/NM/TUE/QM-11/2019 (RP03993G), and Indo-Swedish Joint Research Programme DST/INT/SWD/VR/P-01/2019 (RP04014). B.K.M. acknowledges the funding support from the SERB, DST (Grant No. ECR/2016/001454). The authors thank IIT Delhi HPC facility for computational resources.

[1] C. Liu, Y. Lee, T. Kondo, E. D. Mun, M. Caudle, B. N. Harmon, S. L. Bud'ko, P. C. Canfield, and A. Kaminski, Metallic surface electronic state in half-Heusler compounds *R*PtBi (*R*= Lu, Dy, Gd), Phys. Rev. B **83**, 205133 (2011).

[2] S. Chadov, X. Qi, J. Kübler, G. H. Fecher, C. Felser, and S. C. Zhang, Tunable multifunctional topological insulators in ternary Heusler compounds, Nat. Mater. **9**, 541 (2010).

[3] H. Lin, L. A. Wray, Y. Xia, S. Xu, S. Jia, R. J. Cava, A. Bansil, and M. Z. Hasan, Half-Heusler ternary compounds as new multifunctional experimental platforms for topological quantum phenomena, Nat. Mater. **9**, 546 (2010).

[4] W. Al-Sawai, H. Lin, R. S. Markiewicz, L. A. Wray, Y. Xia, S.-Y. Xu, M. Z. Hasan, and A. Bansil, Topological electronic structure in half-Heusler topological insulators, Phys. Rev. B **82**, 125208 (2010).

[5] Z. Liu, B. Zhou, Y. Zhang, Z. Wang, H. Weng, D. Prabhakaran, S.-K. Mo, Z. Shen, Z. Fang, X. Dai *et al.*, Discovery of a three-dimensional topological Dirac semimetal, Na_3Bi, Science **343**, 864 (2014).

[6] B. Q. Lv, H. M. Weng, B. B. Fu, X. P. Wang, H. Miao, J. Ma, P. Richard, X. C. Huang, L. X. Zhao, G. F. Chen, Z. Fang, X. Dai, T. Qian, and H. Ding, Experimental Discovery of Weyl Semimetal TaAs, Phys. Rev. X **5**, 031013 (2015).

[7] S.-Y. Xu, I. Belopolski, N. Alidoust, M. Neupane, G. Bian, C. Zhang, R. Sankar, G. Chang, Z. Yuan, C.-C. Lee *et al.*, Discovery of a Weyl fermion semimetal and topological Fermi arcs, Science **349**, 613 (2015).

[8] S.-Y. Xu, N. Alidoust, I. Belopolski, Z. Yuan, G. Bian, T.-R. Chang, H. Zheng, V. N. Strocov, D. S. Sanchez, G. Chang *et al.*, Discovery of a Weyl fermion state with Fermi arcs in niobium arsenide, Nat. Phys. **11**, 748 (2015).

[9] L. Fu and C. L. Kane, Superconducting Proximity Effect and Majorana Fermions at the Surface of a Topological Insulator, Phys. Rev. Lett. **100**, 096407 (2008).

[10] H. Yang, J. Yu, S. S. P. Parkin, C. Felser, C.-X. Liu, and B. Yan, Prediction of Triple Point Fermions in Simple Half-Heusler Topological Insulators, Phys. Rev. Lett. **119**, 136401 (2017).

[11] M. Hirschberger, S. Kushwaha, Z. Wang, Q. Gibson, S. Liang, C. A. Belvin, B. A. Bernevig, R. J. Cava, and N. P. Ong, The chiral anomaly and thermopower of Weyl fermions in the half-Heusler GdPtBi, Nat. Mater. **15**, 1161 (2016).

[12] F. Hütt, A. Yaresko, M. B. Schilling, C. Shekhar, C. Felser, M. Dressel, and A. V. Pronin, Linear-in-Frequency Optical Conductivity in GdPtBi due to Transitions Near the Triple Points, Phys. Rev. Lett. **121**, 176601 (2018).

[13] C. Schindler, S. Galeski, W. Schnelle, R. Wawrzyńczak, W. Abdel-Haq, S. N. Guin, J. Kroder, N. Kumar, C. Fu, H. Borrmann *et al.*, Anisotropic electrical and thermal magneto-transport in the magnetic semimetal GdPtBi, Phys. Rev. B **101**, 125119 (2020).

[14] C. Shekhar, N. Kumar, V. Grinenko, S. Singh, R. Sarkar, H. Luetkens, S.-C. Wu, Y. Zhang, A. C. Komarek, E. Kampert *et al.*, Anomalous Hall effect in Weyl semimetal half-Heusler compounds *R*PtBi (*R*= Gd and Nd), Proc. Natl. Acad. Sci. USA **115**, 9140 (2018).

[15] J. Yu, B. Yan, and C.-X. Liu, Model Hamiltonian and time reversal breaking topological phases of antiferromagnetic half-Heusler materials, Phys. Rev. B **95**, 235158 (2017).

[16] B. Yan and C. Felser, Topological materials: Weyl semimetals, Annu. Rev. Condens. Matter Phys. **8**, 337 (2017).

[17] J. Hu, S.-Y. Xu, N. Ni, and Z. Mao, Transport of topological semimetals, Annu. Rev. Mater. Res. **49**, 207 (2019).

[18] N. Kumar, S. N. Guin, C. Felser, and C. Shekhar, Planar Hall effect in the Weyl semimetal GdPtBi, Phys. Rev. B **98**, 041103(R) (2018).

[19] O. Pavlosiuk, D. Kaczorowski, and P. Wiśniewski, Negative longitudinal magnetoresistance as a sign of a possible chiral magnetic anomaly in the half-Heusler antiferromagnet DyPdBi, Phys. Rev. B **99**, 125142 (2019).

[20] O. Pavlosiuk, P. Fałat, D. Kaczorowski, and P. Wiśniewski, Anomalous Hall effect and negative longitudinal magnetoresistance in half-Heusler topological semimetal candidates TbPtBi and HoPtBi, APL Mater. **8**, 111107 (2020).

[21] K. Gofryk, D. Kaczorowski, T. Plackowski, A. Leithe-Jasper, and Y. Grin, Magnetic and transport properties of the rare-earth-based Heusler phases RPd*Z* and RPd_2Z (*Z*= Sb, Bi), Phys. Rev. B **72**, 094409 (2005).

[22] A. Mukhopadhyay, N. Lakshminarasimhan, and N. Mohapatra, Electronic, thermal and magneto-transport properties of the half-Heusler, DyPdBi, Intermetallics **110**, 106473 (2019).

[23] Y. Nakajima, R. Hu, K. Kirshenbaum, A. Hughes, P. Syers, X. Wang, K. Wang, R. Wang, S. R. Saha, D. Pratt *et al.*, Topological RPdBi half-Heusler semimetals: A new family of noncentrosymmetric magnetic superconductors, Sci. Adv. **1**, e1500242 (2015).

[24] V. Bhardwaj, S. P. Pal, L. K. Varga, M. Tomar, V. Gupta, and R. Chatterjee, Weak antilocalization and quantum oscillations of surface states in topologically nontrivial DyPdBi (110) half-Heusler alloy, Sci. Rep. **8**, 9931 (2018).

[25] V. Bhardwaj, A. Bhattacharya, L. K. Varga, A. K. Ganguli, and R. Chatterjee, Thickness-dependent magneto-transport properties of topologically nontrivial DyPdBi thin films, Nanotechnology **31**, 384001 (2020).

[26] G. Kresse and J. Hafner, *Ab initio* molecular dynamics for liquid metals, Phys. Rev. B **47**, 558 (1993).

[27] G. Kresse and J. Furthmüller, Efficiency of *ab initio* total energy calculations for metals and semiconductors using a plane-wave basis set, Comput. Mater. Sci. **6**, 15 (1996).

[28] G. Kresse and J. Furthmüller, Efficient iterative schemes for *ab initio* total-energy calculations using a plane-wave basis set, Phys. Rev. B **54**, 11169 (1996).

[29] P. Giannozzi, S. Baroni, N. Bonini, M. Calandra, R. Car, C. Cavazzoni, D. Ceresoli, G. L. Chiarotti, M. Cococcioni, I. Dabo *et al.*, QUANTUM ESPRESSO: A modular and open-source software project for quantum simulations of materials, J. Phys.: Condens. Matter **21**, 395502 (2009).

[30] P. Giannozzi, O. Andreussi, T. Brumme, O. Bunau, M. B. Nardelli, M. Calandra, R. Car, C. Cavazzoni, D. Ceresoli, M. Cococcioni *et al.*, Advanced capabilities for materials modeling with QUANTUM ESPRESSO, J. Phys.: Condens. Matter **29**, 465901 (2017).

[31] A. Dal Corso, Pseudopotentials periodic table: From H to Pu, Comput. Mater. Sci. **95**, 337 (2014).

[32] M. J. van Setten, M. Giantomassi, E. Bousquet, M. J. Verstraete, D. R. Hamann, X. Gonze, and G.-M. Rignanese, The pseudodojo: Training and grading a 85 element optimized norm-conserving pseudopotential table, Comput. Phys. Commun. **226**, 39 (2018).

[33] K. Lejaeghere, G. Bihlmayer, T. Björkman, P. Blaha, S. Blügel, V. Blum, D. Caliste, I. E. Castelli, S. J. Clark, A. Dal Corso *et al.*, Reproducibility in density functional theory calculations of solids, Science **351**, aad3000 (2016).

[34] J. P. Perdew, K. Burke, and M. Ernzerhof, Generalized Gradient Approximation Made Simple, Phys. Rev. Lett. **77**, 3865 (1996).

[35] K. Gofryk, D. Kaczorowski, T. Plackowski, A. Leithe-Jasper, and Y. Grin, Magnetic and transport properties of rare-earth-based half-Heusler phases RPdBi: Prospective systems for topological quantum phenomena, Phys. Rev. B **84**, 035208 (2011).

[36] M. Topsakal and R. Wentzcovitch, Accurate projected augmented wave (PAW) datasets for rare-earth elements (RE= La–Lu), Comput. Mater. Sci. **95**, 263 (2014).

[37] A. A. Mostofi, J. R. Yates, Y.-S. Lee, I. Souza, D. Vanderbilt, and N. Marzari, WANNIER90: A tool for obtaining maximally-localized Wannier functions, Comput. Phys. Commun. **178**, 685 (2008).

[38] Q. Wu, S. Zhang, H.-F. Song, M. Troyer, and A. A. Soluyanov, WANNIERTOOLS: An open-source software package for novel topological materials, Comput. Phys. Commun. **224**, 405 (2018).

[39] A. Bhattacharya, V. Bhardwaj, B. K. Mani, J. K. Dutt, and R. Chatterjee, Strain-tunable triple point fermions in diamagnetic rare-earth half-Heusler alloys, Sci. Rep. **11**, 12029 (2021).

[40] H. Kim, K. Wang, Y. Nakajima, R. Hu, S. Ziemak, P. Syers, L. Wang, H. Hodovanets, J. D. Denlinger, P. M. Brydon *et al.*, Beyond triplet: Unconventional superconductivity in a spin-3/2 topological semimetal, Sci. Adv. **4**, eaao4513 (2018).

[41] See Supplemental Material at http://link.aps.org/supplemental/10.1103/PhysRevB.107.075144, which includes Refs. [15,42,53–58], for details of the group-theoretical study, Fermi-arc connectivity among topological nodes, and symmetry analysis of AHC and relaxed structures.

[42] H. Zhang, Y. L. Zhu, Y. Qiu, W. Tian, H. B. Cao, Z. Q. Mao, and X. Ke, Field-induced magnetic phase transitions and the resultant giant anomalous Hall effect in the antiferromagnetic half-Heusler compound DyPtBi, Phys. Rev. B **102**, 094424 (2020).

[43] H. V. Gomonay and V. M. Loktev, Spin transfer and current-induced switching in antiferromagnets, Phys. Rev. B **81**, 144427 (2010).

[44] P. Wadley, B. Howells, J. Železn, C. Andrews, V. Hills, R. P. Campion, V. Novák, K. Olejník, F. Maccherozzi, S. Dhesi *et al.*, Electrical switching of an antiferromagnet, Science **351**, 587 (2016).

[45] X. Marti, I. Fina, C. Frontera, J. Liu, P. Wadley, Q. He, R. Paull, J. Clarkson, J. Kudrnovsk, I. Turek *et al.*, Room-temperature antiferromagnetic memory resistor, Nat. Mater. **13**, 367 (2014).

[46] T. Suzuki, R. Chisnell, A. Devarakonda, Y.-T. Liu, W. Feng, D. Xiao, J. W. Lynn, and J. Checkelsky, Large anomalous Hall effect in a half-Heusler antiferromagnet, Nat. Phys. **12**, 1119 (2016).

[47] Y. Zhu, B. Singh, Y. Wang, C.-Y. Huang, W.-C. Chiu, B. Wang, D. Graf, Y. Zhang, H. Lin, J. Sun, A. Bansil, and Z. Mao, Exceptionally large anomalous Hall effect due to anticrossing of spin-split bands in the antiferromagnetic half-Heusler compound TbPtBi, Phys. Rev. B **101**, 161105(R) (2020).

[48] J. Chen, H. Li, B. Ding, P. Chen, T. Guo, X. Xu, D. Zheng, H. Zhang, X. Xi, and W. Wang, Unconventional anomalous Hall effect in the canted antiferromagnetic half-Heusler compound DyPtBi, Adv. Funct. Mater. **32**, 2107526 (2022).

[49] S. S. Tsirkin, High performance Wannier interpolation of Berry curvature and related quantities with WANNIER BERRI code, npj Comput. Mater. **7**, 33 (2021).

[50] Z. L. Sun, K. L. Peng, J. H. Cui, C. S. Zhu, W. Z. Zhuo, Z. Y. Wang, and X. H. Chen, Pressure-controlled anomalous Hall conductivity in the half-Heusler antiferromagnet GdPtBi, Phys. Rev. B **103**, 085116 (2021).

[51] W. Shi, L. Muechler, K. Manna, Y. Zhang, K. Koepernik, R. Car, J. van den Brink, C. Felser, and Y. Sun, Prediction of a magnetic Weyl semimetal without spin-orbit coupling and strong anomalous Hall effect in the Heusler compensated ferrimagnet Ti_2MnAl, Phys. Rev. B **97**, 060406(R) (2018).

[52] A. K. Nayak, J. E. Fischer, Y. Sun, B. Yan, J. Karel, A. C. Komarek, C. Shekhar, N. Kumar, W. Schnelle, J. Kübler *et al.*, Large anomalous Hall effect driven by a nonvanishing Berry curvature in the noncollinear antiferromagnet Mn_3Ge, Sci. Adv. **2**, e1501870 (2016).

[53] H.-R. Trebin, U. Rössler, and R. Ranvaud, Quantum resonances in the valence bands of zinc-blende semiconductors. I. Theoretical aspects, Phys. Rev. B **20**, 686 (1979).

[54] R. Winkler, *Spin-orbit Coupling Effects in Two-dimensional Electron and Hole Systems* (Springer, Berlin, Heidelberg, 2003), Vol. 191.

[55] M. L. Sancho, J. L. Sancho, J. L. Sancho, and J. Rubio, Highly convergent schemes for the calculation of bulk and surface Green functions, J. Phys. F **15**, 851 (1985).

[56] N. Morali, R. Batabyal, P. K. Nag, E. Liu, Q. Xu, Y. Sun, B. Yan, C. Felser, N. Avraham, and H. Beidenkopf, Fermi-arc diversity on surface terminations of the magnetic Weyl semimetal $Co_3Sn_2S_2$, Science **365**, 1286 (2019).

[57] G. Gurung, D.-F. Shao, T. R. Paudel, and E. Y. Tsymbal, Anomalous Hall conductivity of noncollinear magnetic antiperovskites, Phys. Rev. Mater. **3**, 044409 (2019).

[58] C. Le, C. Felser, and Y. Sun, Design strong anomalous Hall effect via spin canting in antiferromagnetic nodal line materials, Phys. Rev. B **104**, 125145 (2021).